FERMILAB-PUB-15-343-AE
(accepted)

Version 1 as of July 21, 2015
Primary authors: Chihway Chang, Vinu Vikram, Bhuvnesh Jain

Wide-Field Lensing Mass Maps from DES Science Verification Data

C. Chang,[1,*] V. Vikram,[2,3] B. Jain,[3] D. Bacon,[4] A. Amara,[1] M. R. Becker,[5,6] G. Bernstein,[3] C. Bonnett,[7] S. Bridle,[8] D. Brout,[3] M. Busha,[5,6] J. Frieman,[9,10] E. Gaztanaga,[11] W. Hartley,[1] M. Jarvis,[3] T. Kacprzak,[1] A. Kovács,[7] O. Lahav,[12] H. Lin,[10] P. Melchior,[13,14] H. Peiris,[12] E. Rozo,[15] E. Rykoff,[6,16] C. Sánchez,[7] E. Sheldon,[17] M. A. Troxel,[8] R. Wechsler,[5,6,16] J. Zuntz,[8] T. Abbott,[18] F. B. Abdalla,[12] S. Allam,[10] J. Annis,[10] A. H. Bauer,[11] A. Benoit-Lévy,[12] D. Brooks,[12] E. Buckley-Geer,[10] D. L. Burke,[6,16] D. Capozzi,[4] A. Carnero Rosell,[19,20] M. Carrasco Kind,[21,22] F. J. Castander,[11] M. Crocce,[11] C. B. D'Andrea,[4] S. Desai,[23] H. T. Diehl,[10] J. P. Dietrich,[23,24] P. Doel,[12] T. F. Eifler,[3,25] A. E. Evrard,[26] A. Fausti Neto,[19] B. Flaugher,[10] P. Fosalba,[11] D. Gruen,[27,28] R. A. Gruendl,[21,22] G. Gutierrez,[10] K. Honscheid,[21,22] D. James,[18] S. Kent,[10] K. Kuehn,[29] N. Kuropatkin,[10] M. A. G. Maia,[19,20] M. March,[3] P. Martini,[13,14] K. W. Merritt,[10] C. J. Miller,[26,30] R. Miquel,[7,31] E. Neilsen,[10] R. C. Nichol,[4] R. Ogando,[19,20] A. A. Plazas,[17,25] A. K. Romer,[32] A. Roodman,[6,16] M. Sako,[3] E. Sanchez,[33] I. Sevilla,[21,33] R. C. Smith,[18] M. Soares-Santos,[10] F. Sobreira,[10,19] E. Suchyta,[13,14] G. Tarle,[23] J. Thaler,[21] D. Thomas,[4,34] D. Tucker,[10] and A. R. Walker[18]

[1]*Department of Physics, ETH Zurich, Wolfgang-Pauli-Strasse 16, CH-8093 Zurich, Switzerland*
[2]*Argonne National Laboratory, 9700 South Cass Avenue, Lemont, IL 60439, USA*
[3]*Department of Physics and Astronomy, University of Pennsylvania, Philadelphia, PA 19104, USA*
[4]*Institute of Cosmology & Gravitation, University of Portsmouth, Portsmouth, PO1 3FX, UK*
[5]*Department of Physics, Stanford University, 382 Via Pueblo Mall, Stanford, CA 94305, USA*
[6]*Kavli Institute for Particle Astrophysics & Cosmology, P. O. Box 2450, Stanford University, Stanford, CA 94305, USA*
[7]*Institut de Física d'Altes Energies, Universitat Autònoma de Barcelona, E-08193 Bellaterra, Barcelona, Spain*
[8]*Jodrell Bank Center for Astrophysics, School of Physics and Astronomy, University of Manchester, Oxford Road, Manchester, M13 9PL, UK*
[9]*Kavli Institute for Cosmological Physics, University of Chicago, Chicago, IL 60637, USA*
[10]*Fermi National Accelerator Laboratory, P. O. Box 500, Batavia, IL 60510, USA*
[11]*Institut de Ciències de l'Espai, IEEC-CSIC, Campus UAB, Facultat de Ciències, Torre C5 par-2, 08193 Bellaterra, Barcelona, Spain*
[12]*Department of Physics & Astronomy, University College London, Gower Street, London, WC1E 6BT, UK*
[13]*Center for Cosmology and Astro-Particle Physics, The Ohio State University, Columbus, OH 43210, USA*
[14]*Department of Physics, The Ohio State University, Columbus, OH 43210, USA*
[15]*University of Arizona, Department of Physics, 1118 E. Fourth St., Tucson, AZ 85721, USA*
[16]*SLAC National Accelerator Laboratory, Menlo Park, CA 94025, USA*
[17]*Brookhaven National Laboratory, Bldg 510, Upton, NY 11973, USA*
[18]*Cerro Tololo Inter-American Observatory, National Optical Astronomy Observatory, Casilla 603, La Serena, Chile*
[19]*Laboratório Interinstitucional de e-Astronomia - LIneA, Rua Gal. José Cristino 77, Rio de Janeiro, RJ - 20921-400, Brazil*
[20]*Observatório Nacional, Rua Gal. José Cristino 77, Rio de Janeiro, RJ - 20921-400, Brazil*
[21]*Department of Physics, University of Illinois, 1110 W. Green St., Urbana, IL 61801, USA*
[22]*National Center for Supercomputing Applications, 1205 West Clark St., Urbana, IL 61801, USA*
[23]*Department of Physics, Ludwig-Maximilians-Universitaet, Scheinerstr. 1, 81679 Muenchen, Germany*
[24]*Excellence Cluster Universe, Boltzmannstr. 2, 85748 Garching, Germany*
[25]*Jet Propulsion Laboratory, California Institute of Technology, 4800 Oak Grove Dr., Pasadena, CA 91109, USA*
[26]*Department of Physics, University of Michigan, Ann Arbor, MI 48109, USA*
[27]*Max Planck Institute for Extraterrestrial Physics, Giessenbachstrasse, 85748 Garching, Germany*
[28]*University Observatory Munich, Scheinerstrasse 1, 81679 Munich, Germany*
[29]*Australian Astronomical Observatory, North Ryde, NSW 2113, Australia*
[30]*Department of Astronomy, University of Michigan, Ann Arbor, MI 48109, USA*
[31]*Institució Catalana de Recerca i Estudis Avançats, E-08010 Barcelona, Spain*
[32]*Department of Physics and Astronomy, Pevensey Building, University of Sussex, Brighton, BN1 9QH, UK*
[33]*Centro de Investigaciones Energéticas, Medioambientales y Tecnológicas (CIEMAT), Madrid, Spain*
[34]*SEPnet, South East Physics Network, (www.sepnet.ac.uk)*

(Dated: July 21, 2015)

We present a mass map reconstructed from weak gravitational lensing shear measurements over 139 deg^2 from the Dark Energy Survey (DES) Science Verification data. The mass map probes both luminous and dark matter, thus providing a tool for studying cosmology. We find good agreement between the mass map and the distribution of massive galaxy clusters identified using a red-sequence cluster finder. Potential candidates for super-clusters and voids are identified using these maps. We measure the cross-correlation between the mass map and a magnitude-limited foreground galaxy sample and find a detection at the 6.8σ level with 20 arcminute smoothing. These measurements are consistent with simulated galaxy catalogs based on ΛCDM N-body simulations, suggesting low systematics uncertainties in the map. We summarize our key findings in this letter; the detailed methodology and tests for systematics are presented in a companion paper.

Operated by Fermi Research Alliance, LLC under Contract No. De-AC02-07CH11359 with the United States Department of Energy.

PACS numbers:

INTRODUCTION

Gravitational lensing refers to the bending of light due to the curvature of space-time induced by massive bodies [1]. This effect allows one to probe the total matter distribution in the Universe, including both luminous and dark matter. Weak lensing is the technique of using the subtle gravitational lensing effect of a large number of galaxies to statistically infer the large-scale matter distribution in the Universe [see 2, 3, for detailed reviews]. The measurement is based on small, percent-level "shears", or distortions of galaxy shapes due to lensing. With several ongoing large optical surveys collecting data [4–7], this technique is one of the most powerful probes for constraining the nature of dark energy [8].

Conventional weak lensing analyses involve calculating the N-point statistics of the shear field. In particular, the *cosmic shear* measurement, which refers to the 2-point correlation function of the shear field in configuration space, has been measured in several earlier datasets [9–14]. Shear γ is defined to be a combination of second derivatives of the lensing potential ψ,

$$\gamma = \gamma_1 + i\gamma_2 = \frac{1}{2}\left(\psi_{,11} - \psi_{,22}\right) + i\psi_{,12}, \tag{1}$$

"$\psi_{,ij} = \partial^2\psi/\partial\theta_i\partial\theta_j$" is the second partial derivative with respect to the angular sky coordinates θ_i of ψ (assuming a spatially flat Universe in the Newtonian limit of GR), which is defined as [15]

$$\psi(\boldsymbol{\theta}, r) = 2\int_0^r \mathrm{d}r' \frac{r - r'}{rr'}\Phi\left(\boldsymbol{\theta}, r'\right). \tag{2}$$

In the above equation, r is the comoving distance and Φ is the 3D gravitational potential, whose spatial structure and time evolution contains cosmological information.

Instead of measuring statistics based on shear, here we focus on an alternative approach by converting shear into the projected density field, the convergence κ, also a combination of second derivatives of ψ,

$$\kappa = \frac{1}{2}\nabla^2\psi = \frac{1}{2}\left(\psi_{,11} + \psi_{,22}\right). \tag{3}$$

The convergence directly represents the integrated mass distribution, which can be seen by using the cosmological Poisson equation and the Limber approximation to re-write Eq. (3) as [2]

$$\kappa(\boldsymbol{\theta}, r) = \frac{3H_0^2\Omega_m}{2}\int_0^r \mathrm{d}r' \frac{r'(r - r')}{r}\frac{\delta\left(\boldsymbol{\theta}, r'\right)}{a(r')}, \tag{4}$$

where H_0 is the Hubble constant today, Ω_m is the total matter density today, a is the cosmological scale factor, and $\delta = (\Delta - \bar{\Delta})/\bar{\Delta}$ is the mass overdensity (Δ and $\bar{\Delta}$ are the 3D density and mean density respectively). In practice we integrate over the redshift distribution of source galaxies as shown in Eq. 15 of the accompanying paper [16].

Note that the same weak lensing effect also introduces distortions in the observed cosmic microwave background (CMB) maps. Reconstructing the convergence map from the CMB gives the integrated mass up to the surface of last scattering ($z \sim 1100$). Compared to the weak lensing convergence map constructed from galaxies, the CMB convergence map typically covers a larger area with lower spatial resolution, and the sources of the lensing effect (the CMB photons) come from a single redshift plane [17–19]. In this letter, we use "weak lensing mass maps" to refer to convergence maps generated from source galaxies.

Weak lensing mass maps supplement measurements based on shear in many ways. Mass maps can be easily cross-correlated with other data since they represent a scalar, the local (projected) mass density, while the shear is a complex variable and is sensitive to the global mass distribution. Cross correlating with X-ray and Sunyaev-Zel'dovich observations helps us understand the relation of hot gas and dark matter in galaxy clusters. Cross correlating with the CMB convergence map provides an important cross check of lensing measurements using different tracers. Other applications of mass maps include peak statistics [20–24], higher-order moments of κ [25], and the identification of superclusters and cosmic voids [26].

The methodology of generating weak lensing mass maps has been demonstrated in earlier work. Massey et al. [27] generated a 3D mass map using COSMOS data in a 1.64 deg^2 area. The high-quality shear measurements and redshift information allow for good mass reconstruction on small scales and in the radial direction. Van Waerbeke et al. [28], on the other hand, focused on larger-scale information and generated 2D wide-field mass maps from four fields of size 25–72 deg^2 in the Canada-France-Hawaii Telescope Lensing Survey (CFHTLenS). Our work is similar to Van Waerbeke et al. [28], but uses one contiguous region of 139 deg^2 from the Dark Energy Survey [DES, 5, 29] data. This is the first step towards building mass maps from the full DES data set.

The data used in this work is part of the Science Verification (SV) dataset from DES, an ongoing ground-based galaxy survey that is scheduled to operate from September 2013 to February 2018. The SV data were collected between November 2012 and February 2013 shortly after the commissioning of the new wide-field mosaic camera, the Dark Energy Camera [DECam, 30–32] on the 4m Blanco telescope at the Cerro Tololo Inter-American Observatory (CTIO) in Chile. This data was used to test survey operations and assess data quality. The images are taken in 5 optical filter bands (*grizY*) on a total area of ~ 250 deg^2 and reach close to the expected full depth of DES at $r \sim 23.9$.

The main goal of this work is to reconstruct the weak lensing mass map from shear measurements of the DES SV

TABLE I: Catalogs and selection criteria used to construct the foreground and background sample for this work, and the number of galaxies in each sample after all the cuts are applied. The redshift cut is based on the mean redshift output from the BPZ photo-z code and the magnitude cut is based on the `MAG_AUTO` parameter in the SExtractor output.

	Background (source)		Foreground (lens)
Input catalog	`ngmix011`	`im3shape`	SVA1 Gold
Photo-z	0.6<z<1.2		0.1<z<0.5
Selection	"conservative additive"		i <22
Number of galaxies	1,111,487	1,013,317	1,106,189
Number density (arcmin^{-2})	2.22	2.03	2.21
Mean redshift	0.826	0.825	0.367

data in a 139 deg^2 contiguous region overlapping with the South Pole Telescope Survey (the SPT-E field). We present the methodology used for the map construction, followed by cross-correlation results and conclusions. Throughout the paper, we adopt the following cosmological parameters: $\Omega_m = 0.3$, $\Omega_\Lambda = 0.7$, $\Omega_k = 0.0$, $h = 0.72$. A detailed account of this work can be found in a companion paper in PRD [16].

METHODOLOGY

Data and simulations

Our galaxy samples are based on the DES SV Gold catalog (Rykoff et al., in preparation) and several extensions to it. The Gold catalog is a product of the DES Data Management [DESDM, 33–36] pipeline version "SVA1" (Yanny et al., in preparation), which includes calibrated photometry and astrometry, object morphology, object classification and masking of the co-add SV images. DESDM utilizes the software packages SCAMP [37], SWARP [38], PSFEx [39] and SExtractor [40] in the pipeline.

Several additional catalogs are used in this work. We use a photometric redshift (photo-z) catalog from the photo-z code Bayesian Photometric Redshifts [BPZ, 41, 42]. We use two shear catalogs from the `ngmix` code [43] and the `im3shape` code [44]. The two independent shear catalogs allows us to assess the robustness of the measurement. The shear measurement algorithms operate on single-exposure images and measure the galaxy shapes, or "ellipticities", by jointly fitting the images of the same galaxies obtained in different exposures with one galaxy model and the different point-spread-function (PSF) model in each image. The resulting ellipticity is a noisy estimator for shear [2]. The shear estimates used in this work have been tested rigorously as described in Jarvis et al. (in preparation).

We extract from these catalogs background ("source") and foreground ("lens") galaxy samples. The objective is to construct the convergence, or mass map, from the background sample and cross-correlate it with the weighted galaxy map built from the foreground sample. Table I lists the final selection criteria for the samples. The foreground sample is magnitude-limited at $i = 22$, while the background sample is selected through a series of lensing tests (Jarvis et al. in preparation) and is not complete. The incompleteness of the background sample affects only the spatial distribution of the noise on these maps but does not bias the signal. In the companion paper we describe in detail the construction of these samples and also discuss a second foreground sample composed of luminous red galaxies (LRGs). Note that the plots in this letter rely on the `ngmix` shear catalog. However we analyzed both shear catalogs to assess their statistical consistency. The "conservative additive" selection criteria on the background sample involves a combination of signal-to-noise (S/N) cuts, size cuts and other quality cuts.

To facilitate our understanding of possible systematics in the procedure of constructing the mass map, we use a set of simulated galaxy catalogs that we match closely to the characteristics of the data (including intrinsic galaxy properties, galaxy number counts, noise, photo-z errors, survey mask). We use the simulated galaxy catalogs developed for the DES collaboration [45]. The catalog is based on three flat ΛCDM dark matter-only N-body simulations with different resolutions. Galaxies are populated using the prescriptions derived from a high-resolution simulation using SubHalo Abundance Matching techniques [45–47]. Photometric properties for each galaxy are then assigned so that the magnitude-color-redshift distribution reproduces that observed in the SDSS DR8 [48] and DEEP2 [49] data. Weak lensing parameters (shear and convergence) are assigned to each galaxy based on the high-resolution ray-tracing algorithm Curved-sky grAvitational Lensing for Cosmological Light conE simulatioNS [50]. Details of the data and simulation catalogs are presented in the companion paper.

Mass and weighted galaxy maps

Eq. (1) and Eq. (3) can be Fourier transformed to get a simple relationship between the Fourier transforms of the shear and convergence, denoted $\hat{\gamma}$ and $\hat{\kappa}$ [51]:

$$\hat{\kappa}_{\boldsymbol{\ell}} = D^*_{\boldsymbol{\ell}} \hat{\gamma}_(\boldsymbol{\ell}), \tag{5}$$

$$D_{\boldsymbol{\ell}} = \frac{\ell_1^2 - \ell_2^2 + 2i\ell_1\ell_2}{|\boldsymbol{\ell}|^2}, \tag{6}$$

where ℓ_i are the components of the angular wavenumber. The above equations hold for $\boldsymbol{\ell} > 0$.

In practice, we pixelate the shear measurements into a map of 5×5 arcmin^2 pixels and Fourier transform the map. We then use Eq. (5) to obtain $\hat{\kappa}$ and inverse Fourier transform to yield our final real-space convergence map. In an ideal scenario, this reconstructed convergence map does not contain an imaginary component. However, due to noise, the finite area of the map, and masking, a non-zero imaginary component is recovered. We separate the real and imaginary parts

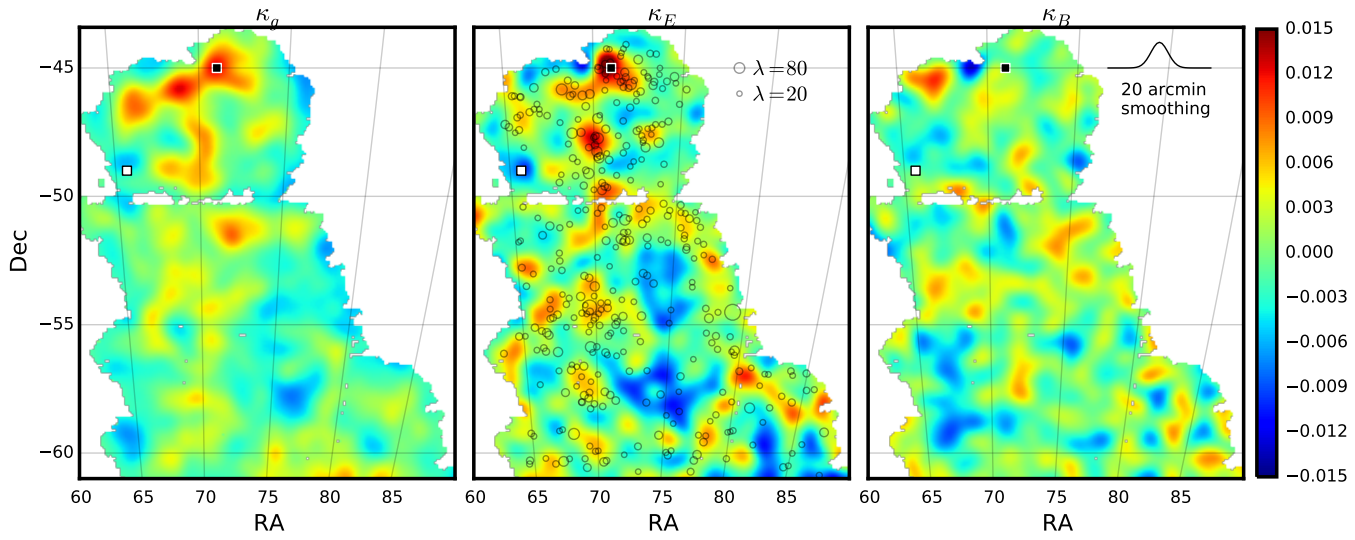

FIG. 1: The DES SV weighted foreground galaxy maps $\kappa_{g,main}$ (left), E-mode convergence map κ_E (middle) and B-mode convergence map κ_B (right) are shown in these panels. All maps are generated with 5×5 arcmin^2 pixels and 20 arcmin RMS Gaussian smoothing. In the κ_g and κ_E maps, red areas corresponds to overdensities and blue areas to underdensities. White regions correspond to the survey mask. The scale of the Gaussian smoothing kernel is indicated by the Gaussian profile on the upper right corner of the right panel. The κ_E map is overlaid by Redmapper galaxy clusters with optical richness $\lambda > 20$. The radius of the circles scale with λ. The black and white squares show the super cluster and super void candidate we investigate in Fig. (2).

of the measured convergence map into E- and B-modes, or $\kappa = \kappa_E + i\kappa_B$. The B-mode convergence is a useful diagnostic tool for testing systematics, as it should vanish for real lensing signals on a sufficiently large area. Finally, as the uncertainty in this reconstruction is formally infinite for a discrete set of noisy shear estimates, it is important to apply a filter to remove the high-frequency noise [52]. In this work we apply a Gaussian filter of different sizes. In the companion paper [16] we use simulations to quantify the degradation in κ_E and the level of κ_B expected from the noise and masking in the data. We find that our results are consistent with that expected from simulations.

One of the main goals of this work is to cross-correlate the mass map with the foreground galaxy distribution. For this purpose, we construct a second mass map assuming that the foreground galaxy sample traces the mass distribution – we refer to this map as κ_g. It is constructed using equation Eq. (4) with δ replaced by δ_g, the fractional overdensity of galaxy counts. Under the assumption of linear bias (i.e. galaxy overdensities are linearly proportional to the total mass overdensities, which is expected to be valid on sufficiently large scales), the smoothed κ_g is simply a product of the mass map κ with a constant bias factor. For our foreground galaxy sample, the linear bias is valid above 5-10 arcmin scales, which is the focus of our study [53]. In practice, the limited redshift range of our foreground galaxy sample means that we cannot expect a perfect estimate of the mass map even if the bias factor were unity.

RESULTS

Fig. (1) shows the resulting weighted galaxy map and the E and B-mode convergence maps generated from the procedure described above. The maps shown are for a Gaussian smoothing of 20 arcmin RMS. We expect κ_E to correlate with κ_g, while κ_B should not correlate with either of the other maps.

Correlation with clusters

The κ_E map shown in the middle panel of Fig. (1) is overlaid with galaxy clusters detected in the same data using the algorithm Redmapper [54]. Each cluster is represented by a circle with radius proportional to the optical richness λ, which is related to mass via a roughly linear relation (see Rykoff et al. [54] for details of the mass calibration of λ). We select only clusters with $\lambda > 20$, which corresponds to mass $\gtrsim 1.7\times10^{14}$ $M_\odot$ ($\lambda = 80$ corresponds to mass $\sim 7.6\times10^{14}$ $M_\odot$). Visually, one can see that the spatial distribution of the clusters traces the mass map very well, with most clusters detected in or around the high κ_E regions.

We analyze the redshift distributions of the clusters in the high and low mass density regions. Two examples are shown in Fig. (2), where we plot (in blue) the lensing efficiency and λ-weighted redshift distribution of the clusters within a 1 degree radius of the identified high and low-mass positions marked in Fig. (1). Compared to the average redshift distribution of clusters (overlaid in grey), we find that the high-mass (low-mass) regions indeed contain many more (fewer) clusters than average. The redshift binning is Δz=0.03, corresponding

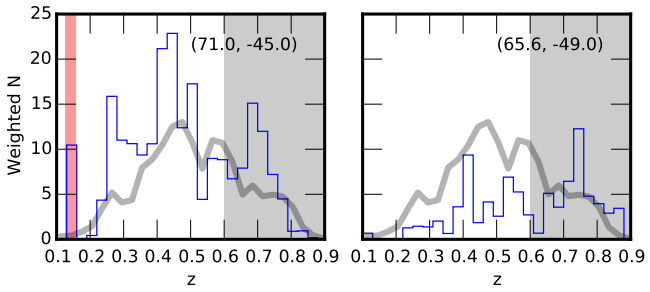

FIG. 2: Blue lines show the richness-weighted redshift distribution of redmapper galaxy clusters along along overdense (left) and underdense (right) regions in the convergence map marked by the black and white squares in Fig. (1). The (RA, Dec) positions of the each region is shown in the upper right corner of each panel. The thick grey line shows the average redshift distribution over the full map. Both lines are weighted by the lensing efficiency. The redshift range above z = 0.6 (marked with the shaded grey area) overlap with the background sample, hence the interpretation of the structures there is more complicated.

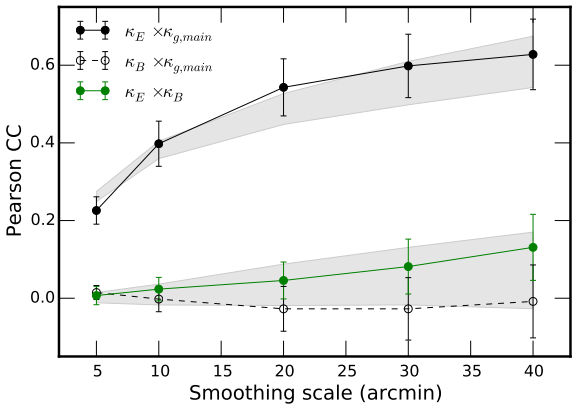

FIG. 3: The Pearson correlation coefficient between the foreground galaxy and convergence maps is shown as a function of smoothing scale. The solid and open symbols show correlation coefficients from the E and B-modes of the convergence respectively. The grey shaded regions show the 1σ bounds from simulations for the correlation between the E and B-mode convergence and the foreground galaxies, with the same pixelization and smoothing as the data as well as sources of statistical uncertainty. The green points show the correlation between E and B-modes of the convergence map. The various correlation coefficients with the B-mode convergence are consistent with zero. Uncertainties on all measurements are estimated using jackknife resampling.

to between 1.5–3 σ_z in this redshift range, where σ_z is the cluster photo-z error uncertainty. The photo-z's for Redmapper clusters are very well determined ($\sigma_z \approx 0.01(1+z)$), which is important for the identifications of the 3D structures. Using these histograms we can identify potential candidates for super-clusters. For example, the peak at $z \sim 0.14$ in the left panel parked in red indicates that this spatial structure is contained in a redshift range localized to within about 100 Mpc along the line of sight. This line of sight has multiple structures at different redshifts, others have just one or two. The redshift range above $z = 0.6$ (marked with the shaded grey area) overlaps with the background sample, hence the interpretation of their relation with the mass map is more complicated. The largest mass concentrations are investigated in more detail in the companion paper and in follow-up studies.

Mass-galaxy correlation

Next, we investigate quantitatively the correlation between the foreground galaxies and the mass map by calculating the Pearson correlation coefficient between the two maps over a range of smoothing scales that span 5 to 40 arcmin. That is, we calculate

$$\rho_{\kappa_E \kappa_g} = \frac{\langle \kappa_E \kappa_g \rangle}{\sigma_{\kappa_E} \sigma_{\kappa_g}}, \tag{7}$$

where $\langle \kappa_E \kappa_g \rangle$ is the covariance between κ_E and κ_g, and σ_{κ_E} and σ_{κ_g} are the standard deviations of the two maps. In this calculation, pixels in the masked region are not used. We also remove pixels within 10 arcmin of the boundaries to avoid significant artefacts from the smoothing. Similarly we calculate the Pearson correlation coefficient between κ_B and the other maps to check for any significant systematic effects. The errors on the correlation coefficients are estimated by a jackknife resampling of 10 deg^2 sub-regions of the maps (each jackknife subsample is $\sim 93\%$ of the total area).

The results are shown in Fig. (3). We find that the Pearson correlation coefficient between κ_g and the E-mode convergence is 0.39 ± 0.06 at 10 arcmin smoothing and 0.52 ± 0.08 at 20 arcmin smoothing. This corresponds to a $\sim 6.8\sigma$ significance at these scales. The correlation between the B-mode convergence and the κ_g maps is consistent with zero at all smoothing scales. The correlation between the E and B-modes convergence is also consistent with zero. The grey shaded regions show the 1σ range of results from the simulated galaxy catalogs modelled to match the main characteristics of the data samples. The black data points agree well with the simulations, suggesting there are no significant contributions to our signal from systematic errors.

To further examine the potential contamination by systematics in the maps, we construct maps of 20 quantities associated with the observing conditions (e.g. airmass, extinction, seeing, PSF ellipticity etc.) and cross correlate with our κ_E and κ_g maps. We find that none of these quantities contribute significantly to the cross correlation signal we have measured, with most of them consistent with zero. Details are presented in the companion paper.

SUMMARY

We present in this letter a weak lensing convergence map generated from shear measurements in the 139 deg^2 SPT-E field in the Dark Energy Survey Science Verification data. The

mean redshift of the source galaxies is 0.82 and corresponds to a comoving distance of 2.9 Gpc. This map probes the projected total mass (luminous and dark), with matter approximately half-way between us and the source galaxies making the most contribution to the lensing. We study the correlation of the mass map with galaxies and clusters that trace the foreground mass distribution.

The spatial distribution of galaxy clusters identified in the same data using an independent technique is highly correlated with the mass map. The combination of the mass map and the cluster catalog provide a powerful tool for exploring potential super-clusters and super-voids in the Universe. Cross-correlating the E-mode mass map with a magnitude-limited foreground galaxy sample gives a 6.8σ detection at 20 arcminute smoothing, while the cross correlation between B-mode mass map and the galaxies is consistent with zero on all scales. The cross-correlation between E and B-mode mass map are also consistent with zero. These results are consistent with simulations of the ΛCDM model in which we have modeled several sources of statistical uncertainties in the lensing and weighted galaxy maps. More detailed analysis, simulation and systematics tests are described in a companion PRD paper [16].

Topics for follow-up studies include the study of galaxy bias, identification of super-clusters and super-voids, higher order moments of the mass map, and cross-correlation with the CMB and other observations. With the full set of data from DES in a few years (~ 35 times the size of the SV data used in this work), we expect the mass maps to be a powerful tool for cosmology.

Acknowledgements

We are grateful for the extraordinary contributions of our CTIO colleagues and the DECam Construction, Commissioning and Science Verification teams in achieving the excellent instrument and telescope conditions that have made this work possible. The success of this project also relies critically on the expertise and dedication of the DES Data Management group.

We thank Jake VanderPlas, Andy Connolly, Phil Marshall, Ludo van Waerbeke and Rafal Szepietowski for discussions and collaborative work on mass mapping methodology. CC and AA are supported by the Swiss National Science Foundation grants 200021-149442 and 200021-143906. SB and JZ acknowledge support from a European Research Council Starting Grant with number 240672. DG was supported by SFB-Transregio 33 'The Dark Universe' by the Deutsche Forschungsgemeinschaft (DFG) and the DFG cluster of excellence 'Origin and Structure of the Universe'. FS acknowledges financial support provided by CAPES under contract No. 3171-13-2. OL acknowledges support from a European Research Council Advanced Grant FP7/291329

Funding for the DES Projects has been provided by the U.S. Department of Energy, the U.S. National Science Foundation, the Ministry of Science and Education of Spain, the Science and Technology Facilities Council of the United Kingdom, the Higher Education Funding Council for England, the National Center for Supercomputing Applications at the University of Illinois at Urbana-Champaign, the Kavli Institute of Cosmological Physics at the University of Chicago, the Center for Cosmology and Astro-Particle Physics at the Ohio State University, the Mitchell Institute for Fundamental Physics and Astronomy at Texas A&M University, Financiadora de Estudos e Projetos, Fundação Carlos Chagas Filho de Amparo à Pesquisa do Estado do Rio de Janeiro, Conselho Nacional de Desenvolvimento Científico e Tecnológico and the Ministério da Ciência e Tecnologia, the Deutsche Forschungsgemeinschaft and the Collaborating Institutions in the Dark Energy Survey.

The DES data management system is supported by the National Science Foundation under Grant Number AST-1138766. The DES participants from Spanish institutions are partially supported by MINECO under grants AYA2012-39559, ESP2013-48274, FPA2013-47986, and Centro de Excelencia Severo Ochoa SEV-2012-0234, some of which include ERDF funds from the European Union.

The Collaborating Institutions are Argonne National Laboratory, the University of California at Santa Cruz, the University of Cambridge, Centro de Investigaciones Energeticas, Medioambientales y Tecnologicas-Madrid, the University of Chicago, University College London, the DES-Brazil Consortium, the Eidgenössische Technische Hochschule (ETH) Zürich, Fermi National Accelerator Laboratory, the University of Edinburgh, the University of Illinois at Urbana-Champaign, the Institut de Ciències de l'Espai (IEEC/CSIC), the Institut de Física d'Altes Energies, Lawrence Berkeley National Laboratory, the Ludwig-Maximilians Universität and the associated Excellence Cluster Universe, the University of Michigan, the National Optical Astronomy Observatory, the University of Nottingham, The Ohio State University, the University of Pennsylvania, the University of Portsmouth, SLAC National Accelerator Laboratory, Stanford University, the University of Sussex, and Texas A&M University.

This paper has gone through internal review by the DES collaboration.

* Electronic address: chihway.chang@phys.ethz.ch

[1] A. Einstein, Science **84**, 506 (1936).
[2] M. Bartelmann and P. Schneider, Physics Reports **340**, 291 (2001), astro-ph/9912508.
[3] H. Hoekstra and B. Jain, Annual Review of Nuclear and Particle Science **58**, 99 (2008), 0805.0139.
[4] K. W. Hodapp, N. Kaiser, H. Aussel, W. Burgett, K. C. Chambers, M. Chun, T. Dombeck, A. Douglas, D. Hafner, J. Heasley, et al., Astronomische Nachrichten **325**, 636 (2004).
[5] B. Flaugher, International Journal of Modern Physics A **20**, 3121 (2005).
[6] S. Miyazaki, Y. Komiyama, H. Nakaya, Y. Kamata, Y. Doi, T. Hamana, H. Karoji, H. Furusawa, S. Kawanomoto, T. Mo-

rokuma, et al. (2012), vol. 8446 of *Proc. SPIE*.

[7] J. T. A. de Jong, G. A. Verdoes Kleijn, K. H. Kuijken, and E. A. Valentijn, Experimental Astronomy **35**, 25 (2013), 1206.1254.

[8] A. Albrecht, G. Bernstein, R. Cahn, W. L. Freedman, J. Hewitt, W. Hu, J. Huth, M. Kamionkowski, E. W. Kolb, L. Knox, et al., ArXiv Astrophysics e-prints: astro-ph/0609591 (2006), arXiv:astro-ph/0609591.

[9] M. Jarvis, B. Jain, G. Bernstein, and D. Dolney, ApJ **644**, 71 (2006), astro-ph/0502243.

[10] H. Lin, S. Dodelson, H.-J. Seo, M. Soares-Santos, J. Annis, J. Hao, D. Johnston, J. M. Kubo, R. R. R. Reis, and M. Simet, ApJ **761**, 15 (2012), 1111.6622.

[11] C. Heymans, L. Van Waerbeke, L. Miller, T. Erben, H. Hildebrandt, H. Hoekstra, T. D. Kitching, Y. Mellier, P. Simon, C. Bonnett, et al., MNRAS **427**, 146 (2012), 1210.0032.

[12] M. J. Jee, J. A. Tyson, M. D. Schneider, D. Wittman, S. Schmidt, and S. Hilbert, ApJ **765**, 74 (2013), 1210.2732.

[13] L. Fu, M. Kilbinger, T. Erben, C. Heymans, H. Hildebrandt, H. Hoekstra, T. D. Kitching, Y. Mellier, L. Miller, E. Semboloni, et al., MNRAS **441**, 2725 (2014), 1404.5469.

[14] M. Kilbinger, L. Fu, C. Heymans, F. Simpson, J. Benjamin, T. Erben, J. Harnois-Déraps, H. Hoekstra, H. Hildebrandt, T. D. Kitching, et al., MNRAS **430**, 2200 (2013), 1212.3338.

[15] A. Joyce, B. Jain, J. Khoury, and M. Trodden, Physics Reports **568**, 1 (2015), 1407.0059.

[16] V. Vikram, C. Chang, B. Jain, D. Bacon, A. Amara, M. R. Becker, G. Bernstein, C. Bonnett, S. Bridle, D. Brout, et al., DE11622 (2015), 1504.03002.

[17] Planck Collaboration, P. A. R. Ade, N. Aghanim, C. Armitage-Caplan, M. Arnaud, M. Ashdown, F. Atrio-Barandela, J. Aumont, C. Baccigalupi, A. J. Banday, et al., A&A **571**, A17 (2014), 1303.5077.

[18] G. P. Holder, M. P. Viero, O. Zahn, K. A. Aird, B. A. Benson, S. Bhattacharya, L. E. Bleem, J. Bock, M. Brodwin, J. E. Carlstrom, et al., ApJ **771**, L16 (2013), 1303.5048.

[19] S. Das, B. D. Sherwin, P. Aguirre, J. W. Appel, J. R. Bond, C. S. Carvalho, M. J. Devlin, J. Dunkley, R. Dünner, T. Essinger-Hileman, et al., Physical Review Letters **107**, 021301 (2011), 1103.2124.

[20] B. Jain and L. Van Waerbeke, ApJ **530**, L1 (2000), astro-ph/9910459.

[21] P. Fosalba, E. Gaztañaga, F. J. Castander, and M. Manera, MNRAS **391**, 435 (2008), 0711.1540.

[22] J. P. Dietrich and J. Hartlap, MNRAS **402**, 1049 (2010), 0906.3512.

[23] J. M. Kratochvil, Z. Haiman, and M. May, Phys.Rev.D **81**, 043519 (2010), 0907.0486.

[24] J. Bergé, A. Amara, and A. Réfrégier, ApJ **712**, 992 (2010), 0909.0529.

[25] L. Van Waerbeke, G. Hinshaw, and N. Murray, Phys.Rev.D **89**, 023508 (2014), 1310.5721.

[26] C. Heymans, M. E. Gray, C. Y. Peng, L. van Waerbeke, E. F. Bell, C. Wolf, D. Bacon, M. Balogh, F. D. Barazza, M. Barden, et al., MNRAS **385**, 1431 (2008), 0801.1156.

[27] R. Massey, J. Rhodes, R. Ellis, N. Scoville, A. Leauthaud, A. Finoguenov, P. Capak, D. Bacon, H. Aussel, J.-P. Kneib, et al., Nature **445**, 286 (2007), astro-ph/0701594.

[28] L. Van Waerbeke, J. Benjamin, T. Erben, C. Heymans, H. Hildebrandt, H. Hoekstra, T. D. Kitching, Y. Mellier, L. Miller, J. Coupon, et al., MNRAS **433**, 3373 (2013), 1303.1806.

[29] The Dark Energy Survey Collaboration, ArXiv Astrophysics e-prints (2005), astro-ph/0510346.

[30] H. T. Diehl and for Dark Energy Survey Collaboration, Physics Procedia **37**, 1332 (2012).

[31] B. L. Flaugher, T. M. C. Abbott, R. Angstadt, J. Annis, M. L. Antonik, J. Bailey, O. Ballester, J. P. Bernstein, R. A. Bernstein, M. Bonati, et al. (2012), vol. 8446 of *Proc. SPIE*, p. 11.

[32] B. Flaugher, H. T. Diehl, K. Honscheid, T. M. C. Abbott, O. Alvarez, R. Angstadt, J. T. Annis, M. Antonik, O. Ballester, L. Beaufore, et al., ArXiv e-prints (2015), 1504.02900.

[33] C. Ngeow, J. J. Mohr, T. Alam, W. A. Barkhouse, C. Beldica, D. Cai, G. Daues, R. Plante, J. Annis, H. Lin, et al. (2006), vol. 6270 of *Proc. SPIE*, p. 23, astro-ph/0608246.

[34] I. Sevilla, R. Armstrong, E. Bertin, A. Carlson, G. Daues, S. Desai, M. Gower, R. Gruendl, W. Hanlon, M. Jarvis, et al., ArXiv e-prints (2011), 1109.6741.

[35] S. Desai, R. Armstrong, J. J. Mohr, D. R. Semler, J. Liu, E. Bertin, S. S. Allam, W. A. Barkhouse, G. Bazin, E. J. Buckley-Geer, et al., ApJ **757**, 83 (2012), 1204.1210.

[36] J. J. Mohr, R. Armstrong, E. Bertin, G. Daues, S. Desai, M. Gower, R. Gruendl, W. Hanlon, N. Kuropatkin, H. Lin, et al. (2012), vol. 8451 of *Proc. SPIE*, 1207.3189.

[37] E. Bertin, in *Astronomical Data Analysis Software and Systems XV*, edited by C. Gabriel, C. Arviset, D. Ponz, and S. Enrique (2006), vol. 351 of *Astronomical Society of the Pacific Conference Series*, p. 112.

[38] E. Bertin, Y. Mellier, M. Radovich, G. Missonnier, P. Didelon, and B. Morin, in *Astronomical Data Analysis Software and Systems XI*, edited by D. A. Bohlender, D. Durand, and T. H. Handley (2002), vol. 281 of *Astronomical Society of the Pacific Conference Series*, p. 228.

[39] E. Bertin, in *Astronomical Data Analysis Software and Systems XX*, edited by I. N. Evans, A. Accomazzi, D. J. Mink, and A. H. Rots (2011), vol. 442 of *Astronomical Society of the Pacific Conference Series*, p. 435.

[40] E. Bertin and S. Arnouts, A&AS **117**, 393 (1996).

[41] N. Benítez, ApJ **536**, 571 (2000), astro-ph/9811189.

[42] D. Coe, N. Benítez, S. F. Sánchez, M. Jee, R. Bouwens, and H. Ford, AJ **132**, 926 (2006), astro-ph/0605262.

[43] E. S. Sheldon, MNRAS **444**, L25 (2014), 1403.7669; downloaded at `https://github.com/esheldon/ngmix`.

[44] J. Zuntz, T. Kacprzak, L. Voigt, M. Hirsch, B. Rowe, and S. Bridle, MNRAS **434**, 1604 (2013), 1302.0183; downloaded at `https://bitbucket.org/joezuntz/im3shape/`.

[45] M. T. Busha, R. H. Wechsler, M. R. Becker, B. Erickson, and A. E. Evrard, in *American Astronomical Society Meeting Abstracts* (2013), vol. 221 of *American Astronomical Society Meeting Abstracts*, p. 341.07.

[46] C. Conroy, R. H. Wechsler, and A. V. Kravtsov, ApJ **647**, 201 (2006), astro-ph/0512234.

[47] R. M. Reddick, R. H. Wechsler, J. L. Tinker, and P. S. Behroozi, ApJ **771**, 30 (2013), 1207.2160.

[48] H. Aihara, C. Allende Prieto, D. An, S. F. Anderson, É. Aubourg, E. Balbinot, T. C. Beers, A. A. Berlind, S. J. Bickerton, D. Bizyaev, et al., ApJS **193**, 29 (2011), 1101.1559.

[49] J. A. Newman, M. C. Cooper, M. Davis, S. M. Faber, A. L. Coil, P. Guhathakurta, D. C. Koo, A. C. Phillips, C. Conroy, A. A. Dutton, et al., ApJS **208**, 5 (2013), 1203.3192.

[50] M. R. Becker, MNRAS **435**, 115 (2013).

[51] N. Kaiser and G. Squires, ApJ **404**, 441 (1993).

[52] L. Van Waerbeke, MNRAS **313**, 524 (2000), astro-ph/9909160.

[53] P. Simon, M. Hetterscheidt, M. Schirmer, T. Erben, P. Schneider, C. Wolf, and K. Meisenheimer, A&A **461**, 861 (2007), astro-ph/0606622.

[54] E. S. Rykoff, B. P. Koester, E. Rozo, J. Annis, A. E. Evrard, S. M. Hansen, J. Hao, D. E. Johnston, T. A. McKay, and R. H. Wechsler, ApJ **746**, 178 (2012), 1104.2089.